

JGR Solid Earth

RESEARCH ARTICLE

10.1029/2020JB020281

Key Points:

- The seafloor topography on the continental shelf of northeast Greenland is estimated from airborne gravity using simulated annealing
- Estimation results reveal a 370–560 m deep trough that allows warm water to reach Zachariæ Isstrøm
- The presence of warm water is observed on both sides of the trough, namely, near the calving front of Zachariæ Isstrøm and in Norske trough

Supporting Information:

- Supporting Information S1

Correspondence to:

J. Yang, Z. Luo and L. Tu,
yang.741@osu.edu;
zcluo@hust.edu.cn;
tlc@hust.edu.cn

Citation:

Yang, J., Luo, Z., & Tu, L. (2020). Ocean access to Zachariæ Isstrøm glacier, Northeast Greenland, revealed by OMG airborne gravity. *Journal of Geophysical Research: Solid Earth*, 125, e2020JB020281. <https://doi.org/10.1029/2020JB020281>

Received 26 MAY 2020

Accepted 7 OCT 2020

Accepted article online 8 OCT 2020

Ocean Access to Zachariæ Isstrøm Glacier, Northeast Greenland, Revealed by OMG Airborne Gravity

Junjun Yang^{1,3} , Zhicai Luo^{1,2} , and Liangcheng Tu^{1,2} 

¹Institute of Geophysics and PGMF, Huazhong University of Science and Technology, Wuhan, China, ²MOE Key Laboratory of Fundamental Physical Quantities Measurement and Hubei Key Laboratory of Gravitation and Quantum Physics, PGMF and School of Physics, Huazhong University of Science and Technology, Wuhan, China, ³State Key Laboratory of Geodesy and Earth's Dynamics, Innovation Academy for Precision Measurement Science and Technology, Chinese Academy of Sciences, Wuhan, China

Abstract Seafloor topography shapes the pathways of ocean currents transporting ocean heat and, thus, is a fundamental boundary condition for modeling ocean-ice interactions. However, few ship bathymetric data are available on the inner continental shelf of northeast Greenland due to the year-round presence of sea ice. We infer seafloor topography of this region from airborne gravity anomaly measured by National Aeronautics and Space Administration's Oceans Melting Greenland (OMG) mission through a nonlinear inversion method called simulated annealing and results in a model with 1.95–3.9 km resolution and 52 m accuracy. The model provides a view of the seafloor near Zachariæ Isstrøm and reveals previously unknown topographic features such as a 370–560 m deep trough that enables warm subsurface water to reach Jøkelbugten fjord into which Zachariæ Isstrøm drains. Present bathymetric models do not show deep enough troughs near Jøkelbugten fjord allowing the inflow of warm water.

1. Introduction

Zachariæ Isstrøm (ZI) and Nioghalvfjerdsfjorden glacier (NG) are two major marine-terminating glaciers in northeast Greenland (see the ice velocity in Figure 1; Joughin et al., 2010). They drain about 198,380 km² in area and hold an ice volume equivalent to 1.1 m global sea level rise (Krieger et al., 2020; Rignot & Mouginot, 2012). After more than 25 years of stability (Khan et al., 2014), ZI started to retreat during the years 2002–2003 and lost 95% of its ice shelf from 2002 to 2012, meanwhile the NG ice shelf, which is only 65 km from ZI, did not undergo such dramatic changes. The calving front of NG retreated by only a few kilometers from 2002 to 2012 (Mouginot et al., 2015, 2019). The variability between the retreat pattern of the two adjacent ice shelves is probably partially caused by local factors like seafloor topography that steers bottom currents (Choi et al., 2017).

The fast retreat of NG and ZI was considered to be partly caused by warm Atlantic water that has been observed in northeast Greenland (Khan et al., 2014; Mayer et al., 2000; Wilson & Straneo, 2015). Seafloor topography shapes the pathways through which ocean currents transport warm Atlantic water from beyond continental shelf to glacial fjords and, thus, is essential for an improved understanding of ice-ocean interaction. Detailed seafloor topography models are required to identify deep troughs that allow the intrusion of warm water toward the glaciers. Bed shapes need to be recognized to explain the evolution of tidewater glaciers, where shallow sills present in deep troughs or fjords are associated with stability (An et al., 2018; Rignot et al., 2016) while retrograde beds (i.e., bed slope deepens inland) are usually linked with rapid retreat (Gudmundsson et al., 2012; Meier & Post, 1987; Millan et al., 2018; Wood et al., 2018). Besides, accurate seafloor topography is a boundary condition for modeling the response of outlet glaciers to ocean forcing, where a higher accuracy leads to a better model performance (De Rydt et al., 2014; Goldberg et al., 2019; Millan et al., 2020; Schodlok et al., 2012). Despite its importance, bathymetric survey tracks are sparse on the inner continental shelf of northeast Greenland, partly due to the presence of icebergs and ice mélange that make ship surveying close to marine-terminating glaciers impossible. Indeed, within 50–100 km of the calving fronts of ZI, the critical zone where warm Atlantic water interacts with the ice shelf, the bathymetric compilation of northeast Greenland (Arndt et al., 2015, 2019) barely contains ship soundings.

In addition to ship soundings, it is possible to infer the seafloor topography from gravity anomaly, because the large density difference between water/ice and bedrock makes the latter contribute most to the short-

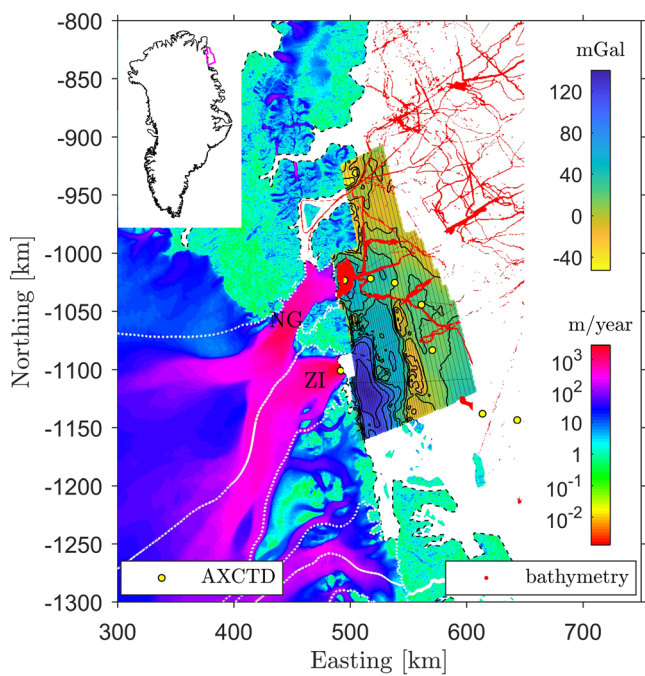


Figure 1. Free-air gravity anomalies measured during OMG mission's northeast campaign (color coded using the upper color bar) overlaid on a map of ice velocity from 2017 to 2018 (color coded on a logarithmic scale using the lower color bar). The thick black lines above the gravity anomalies are contours with 20 mGal interval, and the thin black lines are flight tracks. The dashed black lines are coast boundary. The dotted white lines delineate drainage basins. The red pixels at sea represent bathymetric data extracted from Arndt et al. (2019)'s model. Solid yellow circles represent part of AXCTD instruments deployed by the OMG mission. The location map of the surveyed region is shown in the inset. A similar figure with overlaying bathymetric data removed is shown in Figure S2 for a clearer view of the airborne gravity.

accelerations of the aircraft and the Eötvös effect using differentially-corrected GPS data. Then the latitude correction and free-air correction was applied to yield free-air gravity anomalies. The latitude correction was computed using the International Gravity Formula 1980 (p. 130, Hinze et al., 2013), and the free-air correction was calculated from geodetic latitude and ellipsoidal height using the second-order formula for the GRS80 ellipsoid (p. 133, Hinze et al., 2013). Note that the term “gravity anomaly” in this paper is the “gravity disturbance” as defined in geodesy (Hackney & Featherstone, 2003). Next, the free-air gravity anomalies were filtered with a 28 s half-wavelength low-pass filter to suppress noise, corresponding to an along-track resolution of 1.73 km. The root-mean-square (RMS) of crossover differences of the free-air gravity anomaly data is 1.1 mGal.

The observed free-air gravity anomaly shown in Figure 1 is the combination of the topographic effect, density variations within the Earth, and regional isostatic compensation (i.e., the long-wavelength component of the gravitational acceleration caused by the seafloor topography is partially isostatically compensated; Watts, 2001). The latter two is called the *nontopographic effect*. To infer the seafloor topography, the nontopographic effect should be removed from the observed free-air gravity anomalies prior to the inversion. We adopted An et al. (2019) and Millan et al. (2019)'s data processing technique, that is, we calculated the difference between the observed free-air gravity anomaly and the one forward computed from BedMachine v3 model over areas constrained by bathymetric data (see Figure S3 in the supporting information; Morlighem et al., 2017), AXCTD (Airborne eXpendable Conductivity Temperature Depth) maximum depths (OMG Mission, 2016b), or land surface elevation (Howat et al., 2014) and then interpolated this difference into areas without constraining data using a minimum curvature algorithm (Smith & Wessel, 1990). Then the interpolated difference (Figure S4) was subtracted from the observed free-air gravity anomaly. The

to-intermediate wavelength components of the free-air gravity anomaly (Smith & Sandwell, 1994). From 2015 to 2018, NASA's Oceans Melting Greenland (OMG) mission conducted airborne gravity measurements and bathymetric surveys for key regions of glacial fjords and the inner continental shelves of Greenland. The inner shelves were only sparsely surveyed by the bathymetric ships and depended on complementary dense airborne gravimetry and inversion techniques to efficiently map the seafloor at a reduced resolution (Fenty et al., 2016).

This paper uses the simulated annealing (SA), a global optimization method that can process high-dimensional, nonlinear inverse problems, to estimate the inner continental shelf bathymetry of northeast Greenland from airborne gravity data collected by NASA's OMG mission. We evaluate the accuracy of the inversion using ship soundings extracted from Arndt et al. (2019)'s bathymetric model and discuss the impact of the topographic features identified in the inversion results on the transportation of warm Atlantic water toward the ice shelves and their potential impacts on ocean and ice sheet modeling in the future.

2. Data and Methods

2.1. Airborne Gravity

The airborne gravity was measured by Sander Geophysics Limited (SGL) in July 2016 using Airborne Inertially Referenced Gravimeter (AIRGrav) mounted on a fixed-wing aircraft, Cessna 208B Grand Caravan (OMG Mission, 2016a). The AIRGrav system is capable of conducting draped survey measurements (fly at a consistent height above the ground) of airborne gravity anomalies (Studinger et al., 2008). During the northeast Greenland campaign, the flight altitude ranged from 132 to 1,053 m with a nominal ground clearance of 150 m. The aircraft flew at speeds of about 120 knots with line spacing of 2 km close to the coast versus 4 km farther offshore (see Figure 1). The airborne gravity data were processed by SGL. The raw gravimeter measurements were corrected for the kinematic

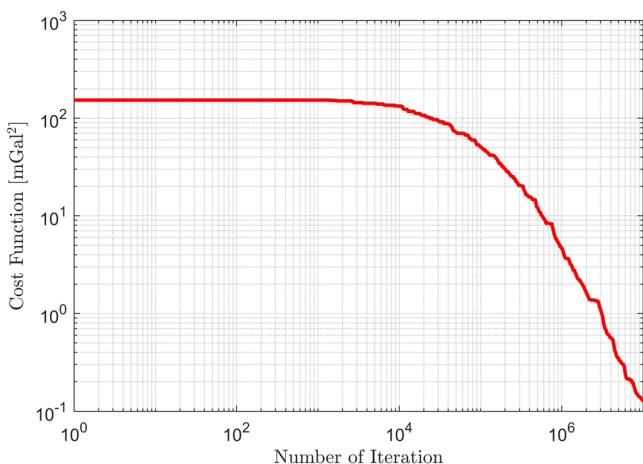


Figure 2. The cost function decreases during the computation.

tainty of gravity estimated seafloor topography. Therefore, the value of these ship sounding data is treated as true depth to evaluate the accuracy of the gravity estimated seafloor topography.

2.3. Gravity Inversion

The process of estimating water depth from airborne gravity is an inversion problem and requires existing constraints and assumptions about the subsurface geology. We employ the very fast simulated annealing (Ingber, 1989) method to estimate the seafloor topography from the pseudo-observed gravity anomaly. The SA method iteratively searches over a set of candidate topographies, with the upper and lower search limits of the unknown seafloor topography set to the bottom of ice layer and 500 m below the seafloor depth value interpolated from BedMachine v3 model, respectively. For a given seafloor topography model in search space, the gravity anomalies are forward computed and compared against the corresponding pseudo-observed gravity anomalies. During the iterations, the SA method can gradually converge to the optimal seafloor topography that minimizes a *cost function*, defined as the average of squared differences between the forward-computed and pseudo-observed gravity anomalies (Yang et al., 2018). The practical implementation of SA for seafloor topography estimation needs to establish the forward model that computes gravity anomaly from a given digital topography model in search space and the cost function, a quality indicator that measures the discrepancy between the forward-computed and pseudo-observed gravity anomalies. We discuss these key steps in section 2.3.1 while refer interested readers to (Yang et al., 2018) for a more detailed description of the SA method.

The SA program was allocated 64 CPU cores from a supercomputer, ran for 32.3 hr, and exited after 1×10^7 iterations. The actual half-wavelength resolution of seafloor topography as estimated through SA is 1.95–3.9 km (see section 2.3.1), but we interpolate the result onto a 150 m × 150 m grid using a cubic interpolation algorithm (Yang, 1986) for consistency with BedMachine v3 model. Then the new grid was filtered through a Gaussian low-pass filter with cutoff wavelength of 3.9 km, since it does not contain information higher than the Nyquist frequency (i.e., half of the sampling rate; Jekeli, 2017) of the original grid.

2.3.1. Forward Model

The gravity anomaly at flight altitude is forward computed using a right rectangular prism (RRP) model. We construct the RRP model by discretizing the volume of the study area into adjacent right rectangular prisms representing three layers of different densities, that is, ice with a density of 916.7 kg/m³ (Morlighem et al., 2017), sea water with a density of 1,028 kg/m³, and bedrock with a density of 2,670 kg/m³ which is consistent with the density of gneiss found in this region (Higgins, 2015). The density of each layer is assumed uniform throughout this study. Since no independent information on sediment thickness is available, we do not model the sediment layer and discuss implications of omission of the sediments to the final result in section 4.2. The identity of each RRP was recognized using the land classification mask in BedMachine v3 model (Morlighem et al., 2017). The RRPs have horizontal dimension of either 1.95 km × 1.95 km or 3.9 km × 3.9 km according to the spacing of flight lines. The coordinates of the horizontal boundaries between adjacent RRPs were known during discretization. The upper or lower boundary

result is referred to as *pseudo-observed gravity anomaly* in the remainder of the paper. It is the input to the inversion model estimating the seafloor topography. The advantage of this technique is that it not only removes the long-wavelength regional gravity but also implicitly takes into account the density variations within the shallow subsurface (Jordan et al., 2020).

2.2. Bathymetric Data

Due to logistical difficulties, OMG mission's bathymetric survey was not conducted in northeast Greenland. The ship soundings used to validate the inversion results are extracted from the bathymetric compilation by Arndt et al. (2019), which contains recently surveyed data that have not been incorporated into IBCAO version 4.0 (Jakobsson et al., 2020). The accuracy of Arndt et al. (2019)'s bathymetric model is not reported. According to the standard S-44 developed by the International Hydrographic Organization (IHO, 2008), the uncertainty of the ship sounding is better than 2% of the water depth (the mean water depth in the study area is 424 m), in general, which is much smaller than the un-

of a RRP represents one of the following surfaces: Earth's surface, ice-water interface, ice-bedrock interface, and seafloor. The surface elevation of Earth, the thickness of the floating and grounded ice, and the depths of the seafloor topography over areas not surveyed by airborne gravimetry were constrained by values interpolated from BedMachine v3 model, whereas the depths of the seafloor topography over areas covered by airborne gravity were treated as unknown parameters.

The gravity anomaly at flight altitude were computed using the aforementioned RRP model. For each computation point, only the prisms within its near zone of radius, 100 km, were used to conduct the forward computation of the gravity anomaly. The *near zone* is defined as the circular area with a preset radius and with its center directly underneath the computation point and the *far zone* as the area outside the near zone. The gravity anomaly at each computation point is the sum of gravitational effect of near zone RRPs. The gravity anomaly due to one RRP was computed using formulas in (Nagy et al., 2000)

$$\delta g = G\rho \left[\frac{-(\xi - x)\ln(\eta - y + r) - (\eta - y)\ln(\xi - x + r) +}{(\zeta - z)\tan^{-1}\frac{(\xi - x)(\eta - y)}{(\zeta - z)r}} \right]_{\xi=x_1}^{x_2} \left|_{\eta=y_1}^{y_2} \right|_{\zeta=z_1}^{z_2}, \quad (1)$$

where G is Newton's gravitational constant, ρ is the density of the RRP, (x, y, z) are the coordinates of the computation point, (ξ, η, ζ) are the variables of integration over the RRP, and $r = \sqrt{(\xi - x)^2 + (\eta - y)^2 + (\zeta - z)^2}$, $[x_1, x_2]$, $[y_1, y_2]$, $[z_1, z_2]$ are the x axis, y axis, and z axis boundaries of the RRP, respectively.

3. Results and Evaluation

3.1. Accuracy Evaluation

During the iterations of SA, the cost function decreases as the iteration number increases. It was 0.13 mGal² at the end of the iteration (Figure 2) and did not reach the theoretical global minimum cost function, 0 mGal². The difference is caused by (1) constraints (e.g., surface elevation and ice thickness) from BedMachine v3 and (2) the large dimensionality of the inversion and the comparatively small number of iterations used. The RMS of the differences with respect to the pseudo-observed gravity anomalies for the ones forward computed using the seafloor topography estimated by SA (see Figure 3a) is 0.42 mGal. The mean of the differences is -0.01 mGal. In comparison, the RMS of the differences between the pseudo-observed gravity anomalies and the one forward computed using the bed elevation grid in BedMachine v3 model (see Figure 3b) is 10.42 mGal.

The ship soundings contained in Arndt et al. (2019)'s bathymetric model were used to evaluate the accuracy of the seafloor topography estimated from airborne gravity using SA. The differences between them were shown in Figure 3c, with a histogram of the differences shown in Figure 3d. The mean of the differences is -7.13 m, and the RMS is 51.56 m. Comparatively large differences occur near the calving front of NG, where the 0.25 km resolution multibeam bathymetric data in (Arndt et al., 2019) reveal sharp variations in seafloor depth. These differences mainly arise from comparison of datasets with different resolutions over rugged areas, because limited by resolution (3.9 km, for places near NG), the airborne gravity is unable to resolve short-wavelength seafloor topographies.

3.2. Seafloor Topography

The new seafloor topography map generated by the SA method is shown in Figure 4. It reveals new features which have never been measured by traditional ship based echo sounders. The most striking feature, delineated by the line b-b' in Figure 4, is a deep trough which connects Norske Trough to Jøkelbugten fjord. The seafloor rises from 593 m deep at point b to 370 m deep at km 14 along b-b', drops to 560 m deep at km 32.5, and stays around this depth for 22 km except at places around km 40 where a 470 m shoal appears (Figure 5). Then the trough gradually rises to 420 m at km 62.5. In the middle of the trough (i.e., from km 62.5 to km 78), most of the seafloor depth ranges from 450 to 460 m. Then the seafloor gradually rises to 370 m at km 85. This is the narrowest place along the profile b-b'. After km 85, the trough widens dramatically and merges with Jøkelbugten fjord. The seafloor slowly deepens to 648 m at km 100 and then sharply deepens to more than 900 m in Jøkelbugten fjord.

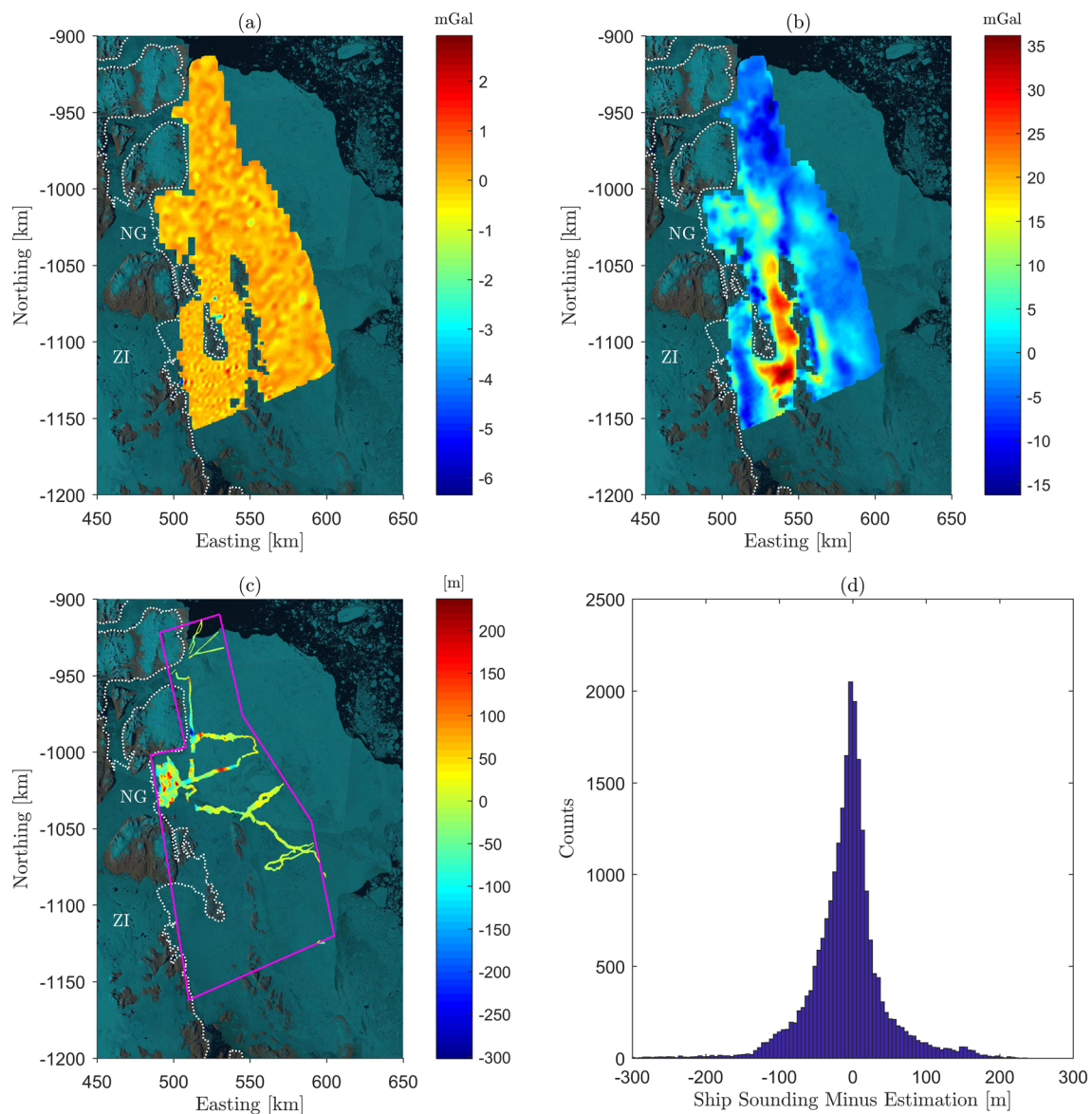


Figure 3. (a) Differences between the pseudo-observed gravity anomalies and the ones forward computed using the seafloor topography estimated by simulated annealing. (b) Differences between the pseudo-observed gravity anomalies and the ones forward computed using the bed elevation grid in BedMachine v3 model. (c) Difference between the bathymetric data contained in Arndt et al. (2019)'s model and the seafloor topography estimated by airborne gravity. (d) The histogram of the difference. The background Landsat 8 image in (a)–(c) was acquired in July 2016, and the white dotted lines are coast boundary.

At the southeast corner of the study area marked by the magenta polygon in Figure 4, the gravity estimated seafloor is 600 m deep. The seafloor becomes shallower northward, until reaches a 370 m shoal around km [555, -1,047]. Then Norske trough deepens northward and becomes 455 m deep at its end around km [553, -1,020]. The gravity estimated seafloor topography reveals a 5 km wide ridge at the end of Norske trough, which is a natural extension of a chain of islands. The profile along the ridge is marked as a-a' in Figure 4 and shown in Figure 5. The deepest point along the profile a-a' is 350 m below sea level.

West of the ridge, near the end of Norske trough are two basins separated by a 5 km wide, 360 m deep sill. The profile that crosses the two basins are marked as c-c' in Figure 4 and shown in Figure 5. East of Hovgaard island, a shoal lies between Westwind trough and Norske trough. The seafloor depth is 160–200 m in the middle and is deeper than 200 m on both sides.

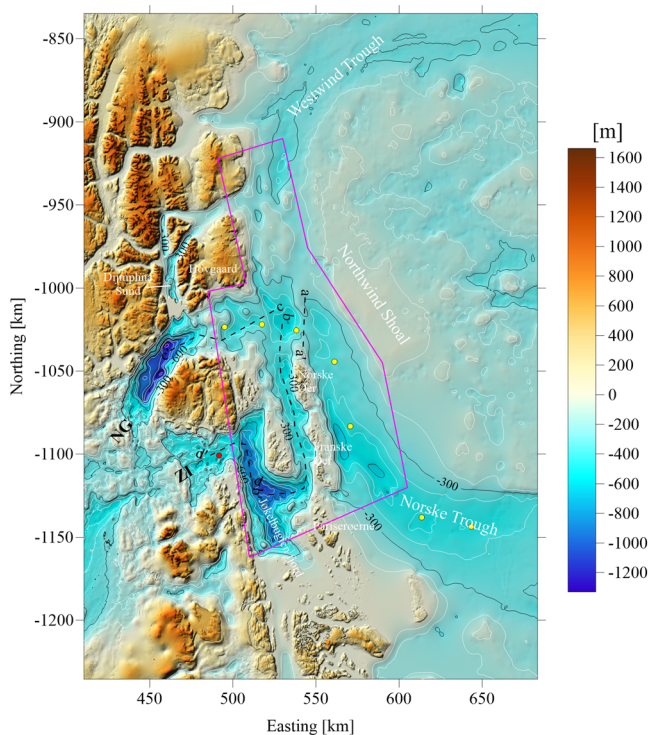


Figure 4. Seafloor depth estimated from airborne gravity through simulated annealing (inside the magenta polygon) and bed elevation from BedMachine v3 model (outside the magenta polygon). All heights in this figure are meters above the EIGEN-6C4 geoid. White lines are minor contours with 100 m interval. Labeled black lines are major contours with 300 m interval. Profiles along a-a' to d-d' are shown in Figure 5. Solid circles represent part of AXCTD instruments deployed by the OMG mission in 2018 (yellow) and 2019 (red). This map uses the polar stereographic projection EPSG 3413 with the scale true at 70°N, origin 90°N, 45°W.

from the continental shelf into the Jøkelbugten fjord into which ZI drains. Some have suggested that ocean warming is the major factor triggering the retreat of ZI (Khan et al., 2014; Mouginot et al., 2015); however, bed elevation of northeast Greenland from BedMachine v3 (Figure S5; red dashed lines along profile b-b' in Figure 5) did not show the existence of pathways of sufficient depth for the inflow of warm water into Jøkelbugten fjord. In northeast Greenland, the seafloor topography in BedMachine v3 model is based on the bathymetric compilation by Arndt et al. (2015). Arndt et al. (2015) produce interpolated surface in areas with sparse ship soundings and thus result in shallow seafloor topography (e.g., 39 to 62 m below sea level along b-b' and south of Jøkelbugten fjord) that would not allow the inflow of warm water. As a consequence, previous modeling of the response of ZI to ocean forcing (Choi et al., 2017) could potentially underestimate the oceanographic influence on ice sheets. We speculate that in addition to reduced buttressing due to the collapse of the ice shelf (Mouginot et al., 2015), the trough along b-b' serving as the pathway for ocean heat also partially contributes to the retreat of ZI since 2002.

Schaffer et al. (2020) conducted the first CTD measurements in the vicinity of ZI, with four measurement points taken inside the trough b-b'. Although not explicitly mentioned, Schaffer et al. (2020)'s analysis of their temperature/depth profiles suggests the existence of the trough along b-b'. Our model supports Schaffer et al. (2020)'s speculation that a sill might exist in km [543, -1,105] because it is the narrowest place along b-b' in Figure 4.

4. Discussion

4.1. Topographic Steering of Ocean Currents

Westwind trough and Norske trough on the comparatively shallow continental shelf are potential pathways for warm Atlantic water to reach the inner shelves. Shallow cold arctic water circulates counterclockwise through the two troughs, whereas the circulation of the deep warm water has not been fully understood (Wilson & Straneo, 2015). Wilson and Straneo (2015) showed that the properties of the water in the cavity beneath NG are consistent with the warm water in Norske trough and are distinct from the warm water in Westwind trough. The shoal to the east of Hovgaard island shown in Figure 4 lends support to Wilson and Straneo (2015)'s hypothesis that the two troughs are separated by a barrier.

The temperature/depth profiles for AXCTD measured on 30 August 2018 along Norske trough (Figure 6a; OMG Mission, 2016b) display the presence of warm Atlantic water. The 1027.82 kg/m³ isopycnal that represents an upper interface of well-mixed Atlantic Intermediate Water (Figure 6c; Schaffer et al., 2020) ranges from 100 to 115 m depth. Waters deeper than 215 m are warmer than 1.5°C, which is more than 3.8°C warmer than the in situ freezing point (Yan et al., 2019) of seawater at 600 m depth, the depth of the calving front of ZI. The AXCTD data reveals a 0.8°C temperature contrast at 250 m depth on either side of the previously unknown sill along a-a', indicating a possible topographic perturbation to the transport of deep waters.

The AXCTD measurements on 25 August 2019 (Figures 6) show the presence of warm water near the calving front of ZI. We find potential pathways of ocean currents transporting warm Atlantic water to the cavity beneath ZI ice shelf. That is, the seafloor topography estimated through SA using airborne gravity reveals a trough along b-b' that is previously unknown until recently (Schaffer et al., 2020). The trough has a minimum depth of 370 m and, thus, could allow intrusion of warm Atlantic water

4.2. Errors Associated With Gravity Inversion Techniques

In section 2.3.1, we explained that the gravity anomaly is forward computed from a discrete topography model within a near zone of 100 km radius. The error at one evaluation point caused by neglecting the far

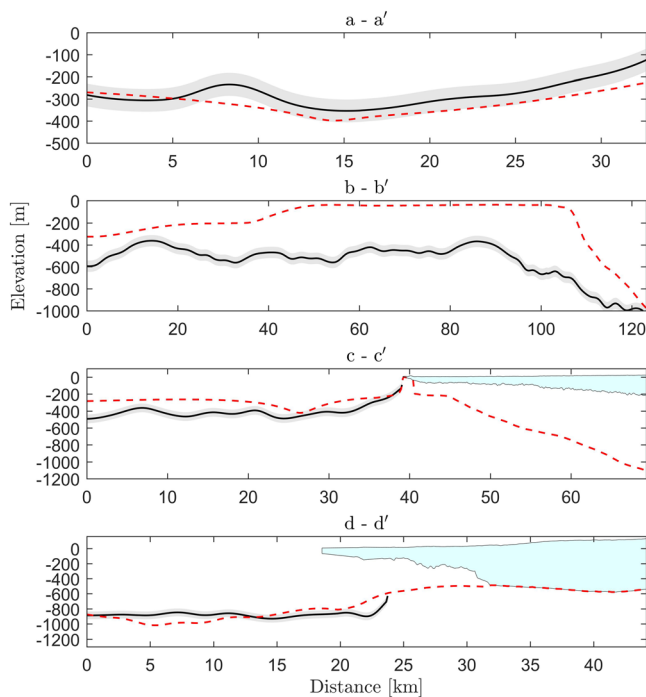


Figure 5. Bed profiles along a-a' to d-d' in Figure 4. The solid black line represents seafloor topography estimated from airborne gravity through simulated annealing with corresponding error bars in shaded gray (\pm RMS), the red dashed lines are the seafloor topography interpolated from the bed elevation in BedMachine v3 model, and light cyan represents ice layer obtained from BedMachine v3 model.

zone effect in the forward computation is defined as the *truncation error*. The *relative truncation error* is defined as the difference between truncation errors of two points separated by a horizontal distance l . Jekeli (2013) developed an algorithmic approach to estimate the relative truncation error in the forward computation of the gravity gradients. This approach was generalized for gravity anomaly and presented in Text S1 in the supporting information. Numerical analysis using the bed elevation in BedMachine v3 model through formula (S1) shows that if the flight altitude is lower than 1 km and the near zone radius is 100 km, the standard deviation of the relative truncation error is smaller than 1.1 mGal (Figure S1), which is in the same level with the observation noise of the gravity anomaly. This means that the gravitational effect of the far zone mass for each computation point is of long-wavelength character. Since the airborne gravity is not sensitive to the seafloor topography at long wavelengths, neglecting the far zone mass does not influence the estimation of seafloor topography.

The study area is adjacent to ZI and NG ice shelves that may change with time. In the gravity inversion, the surface elevation of the floating ice extracted from BedMachine v3 model is from GIMP model (Howat et al., 2014), which approximates the mean elevation over 2003–2009 whereas the airborne gravity was measured in July 2016. Ice shelves in hydrostatic equilibrium do not change the gravity anomaly observed above it (Cochran & Bell, 2012). According to forward computations using surface elevation and ice thickness grids in BedMachine v3, the gravity anomalies caused by the entire ZI and NG ice shelves (i.e., gravity anomalies due to ice shelves not in hydrostatic equilibrium) are 0.02 ± 0.07 mGal, which is smaller than the uncertainty of the gravity measurements. So the temporal changes in surface elevation over the ice shelves are neglected in this study.

Due to lack of independent information on sediments, the inversion method is developed under uniform density assumption for subglacial and subseafloor geology. Although the inconsistency between actual geology and our constant density assumption could be partially accounted for by using An et al. (2019)'s technique (see section 2.1), we acknowledge that away from direct bathymetric observations the errors associated with the density variations increase (Jordan et al., 2020). Through a simple Bouguer plate computation, An et al. (2017) showed that 100 m of sediments with density of $2,200 \text{ kg/m}^3$ leads to 30 m of overestimation in seafloor topography. The variation in bed rock density is similarly assumed to be the largest uncertainty in this study. Another potential error source is the assumption of uniform ice density. Integrating the empirical firn density model (Alley et al., 1982) over a RRP and dividing it by the RRP's volume (Muto et al., 2013) gives the formula for the bulk density of the entire firn/ice column, $\bar{\rho}$. If the ice thickness is 800 m, the presence of firn layer lowers $\bar{\rho}$ to 879.3 kg/m^3 . In the study area, using this ice density instead of 916.7 kg/m^3 only changes the forward-computed gravity anomalies by 0.01 ± 0.04 mGal. So, this study applies no firn correction.

4.3. Difference Between Simulated Annealing and Parker's Method

Several methods have been used in similar regions (An et al., 2017, 2019; Millan et al., 2019; Tinto et al., 2015), among which Parker (1972)'s method is frequently used for 3-D inversion. This study adopted a different method, simulated annealing, so we discuss its difference from the classic Parker's method in this section. First, airplanes loaded with AIRGrav gravimeter fly a draped survey in order to maintain the short-wavelength gravity (Studinger et al., 2008), but Parker's method requires the observed gravity be upward continued to the plane of maximum flight altitude which attenuates the short wavelengths (Jekeli, 1987). Second, Parker's method uses fast Fourier transform so it can only process data on rectangular grids whereas the survey areas of airborne gravity usually are irregular polygons. Patching the observed gravity with the gravity computed from existing low-resolution topography model to form rectangular grids

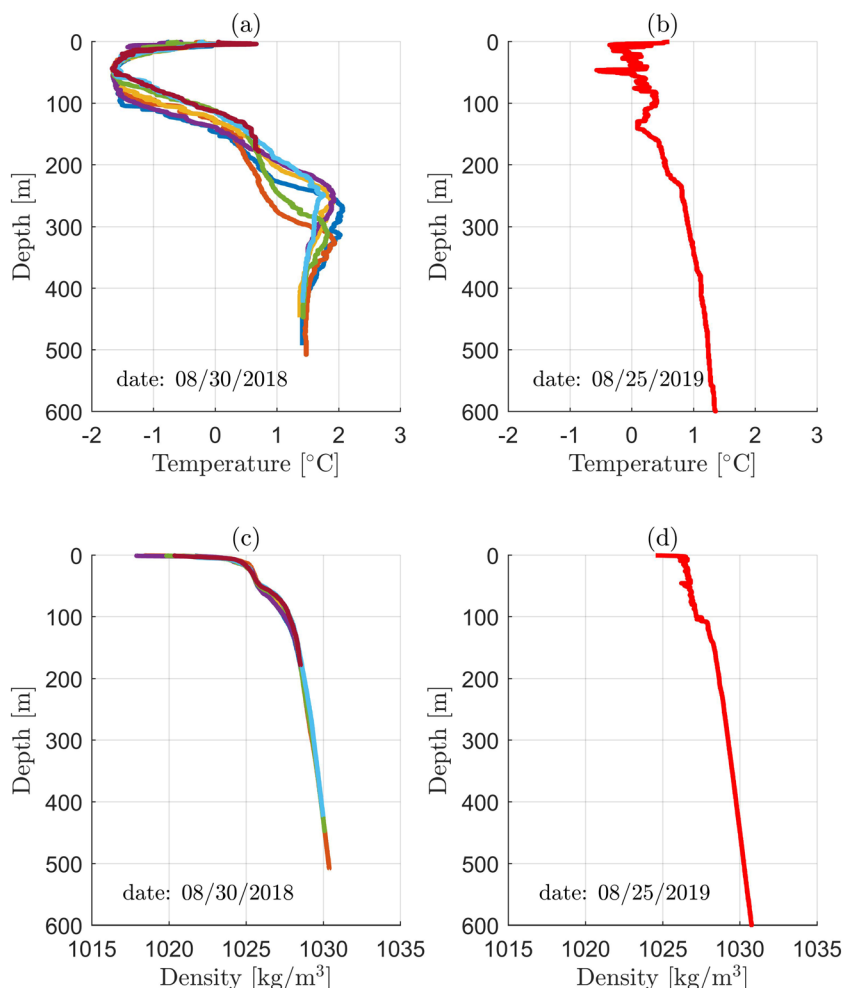


Figure 6. (a, b) Temperature/depth profiles for the AXCTD measurements; (c, d) density/depth profiles for the AXCTD measurements. The location of each AXCTD instrument is shown in Figure 4 using solid circle.

inevitably introduces errors. Third, as concluded by Yang et al. (2018), some researcher's implementation of Parker's method relies on an approximate, linear relationship between seafloor topography and gravity (i.e., use only the first term of Parker's infinite series), which is valid only if the local topography is small compared with the mean sea depth (i.e., in smooth areas); in areas with rugged terrain like that of the NE Greenland region considered here, this linear approximation has the potential to decrease the estimation accuracy by 22% (Yang et al., 2018). Compared with Parker's method, SA completely avoids the linear approximation in the modeled relationship between topography and gravity leading to increased accuracy. Besides, our implementation of SA directly uses observed gravity disturbances along the real flight trajectories. It does not upward continue the gravity disturbance and could use gravity disturbances covering an irregular area. The drawback of SA is its tremendous computational burden. However, Parker's method was developed in 1990s (Smith & Sandwell, 1994). In this era, the computation cost is much cheaper than in the past. It is worthwhile to consider more computationally expensive methods that may improve the estimation accuracy.

5. Conclusions

Along with Petermann, Humboldt, Jakobshavn Isbræ glaciers and Hagen, Sherard Osborn fjords, the ZI and NG sector is one of the marine-based basins in Greenland (Mouginot et al., 2015). Part of the ice sheet in this sector is grounded more than 200 m below sea level until 85 km inland of the grounding line of ZI

(Morlighem et al., 2017). The ocean driven retreat of this sector should be monitored, modeled, and predicted to evaluate its recent and future contribution to global sea level rise (Morlighem et al., 2019). However, the inner continental shelf of northeast Greenland, a critical region where ocean interacts with the ice shelves, is previously modeled by smooth interpolated surface from few ship soundings. We present a reliable view of the seafloor topography in this region that is inferred from the OMG airborne gravity anomalies through simulated annealing. The spatial resolution of the seafloor topography model is 1.95–3.9 km, and the accuracy is 52 m. The results reveal a 370–560 m deep trough that is well below the range of observed warm water depths and provides potential access of warm Atlantic water to ZI. With the refined seafloor topography model, we anticipate an improved performance in the ocean and ice sheet modeling in this region.

Data Availability Statement

The gravity-inferred seafloor topography model will be available at this link (<https://doi.pangaea.de/10.1594/PANGAEA.913524>). It is in NetCDF format which can be read through MATLAB commands “ncdisp” and “ncread.” The simulated annealing program can be downloaded from L. Ingber’s website (<https://www.ingber.com/#ASA>). The airborne gravity data is available at this link (<https://doi.org/10.5067/OMGEV-BTYAG>).

Acknowledgments

The authors are thankful to Josh K. Willis for providing the Oceans Melting Greenland airborne gravity and AXCTD data and to Christopher Jekeli for offering enlightening discussions. Comments from Atsuhiko Muto and Michael Wood were highly appreciated as they led to a significant improvement of the original manuscript. The authors are grateful to the editor, Douglas Schmitt, the anonymous associate editor, and the two anonymous reviewers whose valuable comments significantly improved the presentation of the material. This research was partially supported by grants (42006197, 41931074, 11927812, and 41874089) from National Natural Science Foundation of China, National Key Research and Development Program of China (2018YFC1503503), and a grant (SKLGED2020-1-1-E) from State Key Laboratory of Geodesy and Earth’s Dynamics.

References

- Alley, R. B., Bolzan, J. F., & Whillans, I. M. (1982). Polar firn densification and grain growth. *Annals of Glaciology*, 3, 7–11. <https://doi.org/10.1017/S0260305500002433>
- An, L., Rignot, E., Elieff, S., Morlighem, M., Millan, R., Mouginot, J., et al. (2017). Bed elevation of Jakobshavn Isbræ, West Greenland, from high-resolution airborne gravity and other data. *Geophysical Research Letters*, 44, 3728–3736. <https://doi.org/10.1002/2017GL073245>
- An, L., Rignot, E., Millan, R., Tinto, K., & Willis, J. (2019). Bathymetry of Northwest Greenland using “Ocean Melting Greenland” (OMG) high-resolution airborne gravity and other data. *Remote Sensing*, 11, 131–147. <https://doi.org/10.3390/rs11020131>
- An, L., Rignot, E., Mouginot, J., & Millan, R. (2018). A century of stability of Avannarleq and Kujalleq Glaciers, West Greenland, explained using high-resolution airborne gravity and other data. *Geophysical Research Letters*, 45, 3156–3163. <https://doi.org/10.1002/2018GL07204>
- Arndt, J. E., Callard, S. L., Dorschel, B., Grob, H., Kanzow, T., Kappelsberger, M., et al. (2019). An update to the Northeast Greenland—Digital bathymetric compilation. PANGAEA. <https://doi.org/10.1594/PANGAEA.909628>
- Arndt, J. E., Jokat, W., Dorschel, B., Myklebust, R., Dowdeswell, J. A., & Evans, J. (2015). A new bathymetry of the Northeast Greenland continental shelf: Constraints on glacial and other processes. *Geochemistry, Geophysics, Geosystems*, 16, 3733–3753. <https://doi.org/10.1002/2015GC005931>
- Choi, Y., Morlighem, M., Rignot, E., Mouginot, J., & Wood, M. (2017). Modeling the response of Nioghalvfjerdssjorden and Zachariae Isstrom glaciers, Greenland, to ocean forcing over the next century. *Geophysical Research Letters*, 44, 11,071–11,079. <https://doi.org/10.1002/2017gl075174>
- Cochran, J. R., & Bell, R. E. (2012). Inversion of IceBridge gravity data for continental shelf bathymetry beneath the Larsen ice shelf, Antarctica. *Journal of Glaciology*, 58(209), 540–552. <https://doi.org/10.3189/2012JoG11J033>
- De Rydt, J., Holland, P. R., Dutrieux, P., & Jenkins, A. (2014). Geometric and oceanographic controls on melting beneath Pine Island glacier. *Journal of Geophysical Research: Oceans*, 119, 2420–2438. <https://doi.org/10.1002/2013jc009513>
- Fenty, I., Willis, J. K., Khazendar, A., Dinardo, S., Forsberg, R., Fukumori, I., et al. (2016). Oceans Melting Greenland: Early results from NASA’s ocean-ice mission in Greenland. *Oceanography*, 29, 72–83. <https://doi.org/10.5670/oceanog.2016.100>
- Goldberg, D. N., Gourmelen, N., Kimura, S., Millan, R., & Snow, K. (2019). How accurately should we model ice shelf melt rates? *Geophysical Research Letters*, 46, 189–199. <https://doi.org/10.1029/2018GL080383>
- Gudmundsson, G. H., Krug, J., Durand, G., Favier, L., & Gagliardini, O. (2012). The stability of grounding lines on retrograde slopes. *The Cryosphere*, 6(6), 1497–1505. <https://doi.org/10.5194/tc-6-1497-2012>
- Hackney, R. I., & Featherstone, W. E. (2003). Geodetic versus geophysical perspectives of the ‘gravity anomaly’. *Geophysical Journal International*, 154(1), 35–43. <https://doi.org/10.1046/j.1365-246X.2003.01941.x>
- Higgins, A. K. (2015). *Descriptive Text to the Geological Map of Greenland, 1:500 000, Lambert Land, Sheet 9*. Albertslund, Denmark: Geological Survey of Denmark and Greenland.
- Hinze, W. J., Von Frese, R. R. B., & Saad, A. H. (2013). *Gravity and Magnetic Exploration: Principles, Practices, and Applications*. New York: Cambridge University Press. <https://doi.org/10.1017/CBO9780511843129>
- Howat, I. M., Negrete, A., & Smith, B. E. (2014). The Greenland Ice Mapping Project (GIMP) land classification and surface elevation data sets. *The Cryosphere*, 8, 1509–1518. <https://doi.org/10.5194/tc-8-1509-2014>
- IHO (2008). *IHO Standards for Hydrographic Surveys (S-44)* (5th ed.). Monaco: International Hydrographic Bureau.
- Ingber, L. (1989). Very fast simulated re-annealing. *Mathematical and Computer Modelling*, 12(8), 967–973. [https://doi.org/10.1016/0895-7177\(89\)90202-1](https://doi.org/10.1016/0895-7177(89)90202-1)
- Jakobsson, M., Mayer, L. A., Bringensparr, C., Castro, C. F., Mohammad, R., Johnson, P., et al. (2020). The international bathymetric chart of the Arctic Ocean version 4.0. *Scientific Data*, 7, 176. <https://doi.org/10.1038/s41597-020-0520-9>
- Jekeli, C. (1987). The downward continuation of aerial gravimetric data without density hypothesis. *Bulletin Geodesique*, 61(4), 319–329. <https://doi.org/10.1007/bf02520558>
- Jekeli, C. (2013). Extent and resolution requirements for the residual terrain effect in gravity gradiometry. *Geophysical Journal International*, 195, 211–221. <https://doi.org/10.1093/gji/ggt246>

- Jekeli, C. (2017). *Spectral Methods in Geodesy and Geophysics*. Boca Raton, FL: CRC Press. <https://doi.org/10.1201/9781315118659>
- Jordan, T. A., Porter, D., Tinto, K., Millan, R., Muto, A., Hogan, K., et al. (2020). New gravity-derived bathymetry for the Thwaites, Crosson and Dotson ice shelves revealing two ice shelf populations. *The Cryosphere Discussions*, 1–20. <https://doi.org/10.5194/tc-2019-294>
- Joughin, I., Smith, B. E., Howat, I. M., Scambos, T., & Moon, T. (2010). Greenland flow variability from ice-sheet-wide velocity mapping. *Journal of Glaciology*, 56(197), 415–430. <https://doi.org/10.3189/002214310792447734>
- Khan, S. A., Kjær, K. H., Bevis, M., Bamber, J. L., Wahr, J., Kjeldsen, K. K., et al. (2014). Sustained mass loss of the Northeast Greenland ice sheet triggered by regional warming. *Nature Climate Change*, 4, 292–299. <https://doi.org/10.1038/nclimate2161>
- Krieger, L., Floricioiu, D., & Neckel, N. (2020). Drainage basin delineation for outlet glaciers of Northeast Greenland based on Sentinel-1 ice velocities and TanDEM-X elevations. *Remote Sensing of Environment*, 237, 111483. <https://doi.org/10.1016/j.rse.2019.111483>
- Mayer, C., Reeh, N., Jung-Rothenhäusler, F., Huybrechts, P., & Oerter, H. (2000). The subglacial cavity and implied dynamics under Nioghalvfjerdsfjorden Glacier, NE-Greenland. *Geophysical Research Letters*, 27(15), 2289–2292. <https://doi.org/10.1029/2000GL011514>
- Meier, M. F., & Post, A. (1987). Fast tidewater glaciers. *Journal of Geophysical Research*, 92(B9), 9051–9058. <https://doi.org/10.1029/JB092iB09p09051>
- Millan, R., Rignot, E., Mouginot, J., Wood, M., Bjork, A. A., & Morlighem, M. (2018). Vulnerability of Southeast Greenland glaciers to warm Atlantic water from Operation IceBridge and Ocean Melting Greenland data. *Geophysical Research Letters*, 45, 2688–2696. <https://doi.org/10.1029/2017GL076561>
- Millan, R., Rignot, E., Rivera, A., Martineau, V., Mouginot, J., Zamora, R., et al. (2019). Ice thickness and bed elevation of the Northern and Southern Patagonian Icefields. *Geophysical Research Letters*, 46, 6626–6635. <https://doi.org/10.1029/2019GL082485>
- Millan, R., St-Laurent, P., Rignot, E., Morlighem, M., Mouginot, J., & Scheuchl, B. (2020). Constraining an ocean model under Getz Ice Shelf, Antarctica, using a gravity-derived bathymetry. *Geophysical Research Letters*, 47, e2019GL086522. <https://doi.org/10.1029/2019GL086522>
- Mission, O. M. G. (2016a). *Airborne Gravity Data from the Airborne Bathymetry Survey, ver. 0.1*. CA, USA: OMG SDS. <https://doi.org/10.5067/OMGEV-BTYAG>
- Mission, O. M. G. (2016b). *Conductivity, Temperature and Depth (CTD) Data from the Ocean Survey, Ver. 0.1*. CA, USA: OMG SDS. <https://doi.org/10.5067/OMGEV-AXCTD>
- Morlighem, M., Williams, C. N., Rignot, E., An, L., Arndt, J. E., Bamber, J. L., et al. (2017). BedMachine v3: Complete bed topography and ocean bathymetry mapping of Greenland from multibeam echo sounding combined with mass conservation. *Geophysical Research Letters*, 44, 11,051–11,061. <https://doi.org/10.1002/2017GL074954>
- Morlighem, M., Wood, M., Seroussi, H., Choi, Y., & Rignot, E. (2019). Modeling the response of Northwest Greenland to enhanced ocean thermal forcing and subglacial discharge. *The Cryosphere*, 13, 723–734. <https://doi.org/10.5194/tc-13-723-2019>
- Mouginot, J., Rignot, E., Bjork, A. A., van den Broeke, M., Millan, R., Morlighem, M., et al. (2019). Forty-six years of Greenland Ice Sheet mass balance from 1972 to 2018. *Proceedings of the National Academy of Sciences*, 116, 9239–9244. <https://doi.org/10.1073/pnas.1904242116>
- Mouginot, J., Rignot, E., Scheuchl, B., Fenty, I., Khazendar, A., Morlighem, M., et al. (2015). Fast retreat of Zachariae Isstrøm, Northeast Greenland. *Science*, 350, 1357–1361. <https://doi.org/10.1126/science.aac7111>
- Muto, A., Christianson, K., Horgan, H. J., Anandakrishnan, S., & Alley, R. B. (2013). Bathymetry and geological structures beneath the Ross Ice Shelf at the mouth of Whillans Ice Stream, West Antarctica, modeled from ground-based gravity measurements. *Journal of Geophysical Research: Solid Earth*, 118, 4535–4546. <https://doi.org/10.1002/jgrb.50315>
- Nagy, D., Papp, G., & Benedek, J. (2000). The gravitational potential and its derivatives for the prism. *Journal of Geodesy*, 74(7–8), 552–560. <https://doi.org/10.1007/s001900000116>
- Parker, R. L. (1972). The rapid calculation of potential anomalies. *Geophysical Journal of the Royal Astronomical Society*, 31(4), 447–455. <https://doi.org/10.1111/j.1365-246X.1973.tb06513.x>
- Rignot, E., Fenty, I., Xu, Y., Cai, C., Velicogna, I., Cofaigh, C. Ó., et al. (2016). Bathymetry data reveal glaciers vulnerable to ice-ocean interaction in Uummannaq and Vaigat glacial fjords, West Greenland. *Geophysical Research Letters*, 43, 2667–2674. <https://doi.org/10.1002/2016GL067832>
- Rignot, E., & Mouginot, J. (2012). Ice flow in Greenland for the international polar year 2008–2009. *Geophysical Research Letters*, 39, L11501. <https://doi.org/10.1029/2012GL051634>
- Schaffer, J., Kanzow, T., von Appen, W.-J., von Albedyll, L., Arndt, J. E., & Roberts, D. H. (2020). Bathymetry constrains ocean heat supply to Greenland's largest glacier tongue. *Nature Geoscience*, 13, 227–231. <https://doi.org/10.1038/s41561-019-0529-x>
- Schedlak, M. P., Menemenlis, D., Rignot, E., & Studinger, M. (2012). Sensitivity of the ice-shelf/ocean system to the sub-ice-shelf cavity shape measured by NASA Ice Bridge in Pine Island Glacier, West Antarctica. *Annals of Glaciology*, 53(60), 156–162. <https://doi.org/10.3189/2012AoG60A073>
- Smith, W. H. F., & Sandwell, D. T. (1994). Bathymetric prediction from dense satellite altimetry and sparse shipboard bathymetry. *Journal of Geophysical Research*, 99(B11), 21,803–21,824. <https://doi.org/10.1029/94JB00988>
- Smith, W. H. F., & Wessel, P. (1990). Gridding with continuous curvature splines in tension. *Geophysics*, 55(3), 293–305. <https://doi.org/10.1190/1.1442837>
- Studinger, M., Bell, R., & Frearson, N. (2008). Comparison of AIRGrav and GT-1A airborne gravimeters for research applications. *Geophysics*, 73(6), I51–I61. <https://doi.org/10.1190/1.2969664>
- Tinto, K. J., Bell, R. E., Cochran, J. R., & Münchow, A. (2015). Bathymetry in Petermann fjord from Operation IceBridge aerogravity. *Earth and Planetary Science Letters*, 422, 58–66. <https://doi.org/10.1016/j.epsl.2015.04.009>
- Watts, A. B. (2001). *Isostasy and Flexure of the Lithosphere*. Cambridge, UK: Cambridge University Press.
- Wilson, N. J., & Straneo, F. (2015). Water exchange between the continental shelf and the cavity beneath Nioghalvfjerdsbræ (79 North Glacier). *Geophysical Research Letters*, 42, 7648–7654. <https://doi.org/10.1002/2015GL064944>
- Wood, M., Rignot, E., Fenty, I., Menemenlis, D., Millan, R., Morlighem, M., et al. (2018). Ocean-induced melt triggers glacier retreat in Northwest Greenland. *Geophysical Research Letters*, 45, 8334–8342. <https://doi.org/10.1029/2018GL078024>
- Yan, L., Wang, Z., Liu, C., & Wu, Y. (2019). On the determination and simulation of seawater freezing point temperature under high pressure. *Advances in Polar Science*, 30, 391–398. <https://doi.org/10.13679/j.advps.2019.0018>
- Yang, J., Jekeli, C., & Liu, L. (2018). Seafloor topography estimation from gravity gradients using simulated annealing. *Journal of Geophysical Research: Solid Earth*, 123, 6958–6975. <https://doi.org/10.1029/2018JB015883>
- Yang, T. Y. (1986). *Finite Element Structural Analysis*. Englewood Cliffs, New York: Prentice Hall.